This is a repository copy of *Relationships between the electrical properties and nanostructure of soot particles in a laminar inverse diffusion flame*.

White Rose Research Online URL for this paper:
https://eprints.whiterose.ac.uk/172714/

Version: Accepted Version

Article:

Relationships between the electrical properties and nanostructure of soot particles in a laminar inverse diffusion flame

Ye Liu, Chonglin Song*, Gang Lv, Chenyang Fan, Xuyang Zhang, Yuehan Qiao

State Key Laboratory of Engines, Tianjin University, Tianjin 300072, China

* **Corresponding author:**
   • Mailing address: State Key Laboratory of Engines, Tianjin University, Tianjin 300072, P. R. China
   • Fax: +86-22-27403750; Tel.: +86-22-27406840-8020
   • Email: songchonglin@tju.edu.cn (C.-L. Song)

Colloquium:
   2. SOOT, NANOMATERIALS, AND LARGE MOLECULES

Total length of paper and method of determination:
   Method 1: 6192

Word equivalent lengths:
   Main text: 3953
   Nomenclature: 0
   Equations: 60
   Eq. (1): 30; Eq. (2): 30
   References: 734
   Figures with captions: 1225
   Fig. 1: 227; Fig. 2: 145; Fig. 3: 149; Fig. 4: 143; Fig. 5: 144; Fig. 6: 138; Fig. 7: 140; Fig. 8: 139
   Tables: 220
   Table 1: 61; Table 2: 106; Table 3:53

Affirmation to pay color reproduction charges if applicable:
   No color reproduction, print in grey scale

Relationships between the electrical properties and nanostructure of soot particles in a laminar inverse diffusion flame

Ye Liu, Chonglin Song*, Gang Lv, Chenyang Fan, Xuyang Zhang, Yuehan Qiao

State Key Laboratory of Engines, Tianjin University, Tianjin 300072, China

Abstract: This paper studies the electrical properties of the soot particles generated from an n-heptane inverse diffusion flame and the relationship between the electrical properties and the nanostructure. The electrical conductivity of isolated soot particle and work function of soot particles were measured by a PeakForce tunneling atomic force microscopy and a Kelvin-probe force microscopy. The nanostructure of soot particles was evaluated using X-ray diffraction and X-ray photoelectron spectroscopy. Different electrical conductivity distributions were found as the soot particles gradually matured, and at the same time the mean electrical conductivity of soot particles exhibited a nearly exponential increase. There existed a percolation threshold at which the mean electrical conductivity sharply increased by approximately two orders of magnitude. Similarly, the work function of soot particles increased during soot maturation process, which implies that it becomes harder for the electrons to escape from the soot samples. The crystallite width had a positive correlation with the logarithm of electrical conductivity and the work function for soot particles, while the interlayer spacing presented a negative correlation with the logarithm of electrical conductivity and work function. These results suggest that the electrical conductivity and work function can serve as indicators of ordering degree of soot particles. Moreover, the dependence of electrical properties on the nanostructure demonstrates the potential of better controlled flame conditions for producing tailored soot particles for a variety of applications.

1. Introduction

Recently, there has been substantial interest in the electrical properties of various carbon materials, including graphene, carbon nanotubes and carbon black, because of their applications in many technical areas [1-5]. Here, the term "electrical properties" refers to the electrical conductivity and work function. Electrical conductivity is a key parameter in applications such as electronic components, cables, and electrodes [1,6]. The work function can be regarded as the difference in energy between the vacuum level and the most loosely bound electrons inside the carbon material [7]. The work function is of great importance for understanding the electronic functions of carbon materials, thereby making it essential for the fabrication of high-performance engineered electronic devices [3].

The correlations between the electrical property and structure for carbon materials have been studied by several researchers. Odom et al. [8] reported that carbon nanotubes with metallic or semiconducting property were depended on the helicity of the arrangement of graphitic rings in their walls. Yao et al. [4] showed that the difference in the electrical conductivity of single-wall carbon nanotubes could be a consequence of the variation in the internal structure. Rhim et al. [2] observed that the microcrystalline cellulose underwent a transformation from amorphous structure to more orderly graphitic structure during the heat treatment, which gave rise to an increase in the electrical conductivity.

Flame-generated soot is a type of carbon material with more content of amorphous carbon than other carbon materials, including graphene, nanotube and carbon blacks. Thus, flame-generated soot possesses substantially different structure from other carbon materials [9,10], which in turn probably exhibits different electrical properties. To date, information concerning the relationships between the electrical properties and the nanostructure is limited for the flame-generated soot. In this context, the

present paper investigates the electrical properties and nanostructure of the flame-generated soot

particles. A thermophoretic sampling technique and a probe sampling technique were employed to

obtain soot particles generated from a laminar n-heptane inverse diffusion flame. The electrical

conductivity of an isolated soot particle was measured by a novel PeakForce tunneling atomic force

microscopy (PF-TUNA) technique. The work function of soot particles was assessed by a Kelvin-

probe force microscopy (KPFM) technique. The structural features of the soot particles were analyzed

by X-ray diffraction (XRD), X-ray photoelectron spectroscopy (XPS), and high-resolution

transmission electron microscopy (HRTEM). Moreover, correlations between the electrical properties

and the nanostructure of flame-generated soot particles were investigated.

2. Experimental setup

*2.1. Burner and sampling system*

The schematic diagram of the experimental system is shown in Fig. S1 of Supplemental material.

The inverse diffusion flame burner used in this study was similar to those used by Blevins et al. [11]

and Santamaria et al. [12]. The burner was a center-tube McKenna burner (Holthius & Associates)

with a center tube for a mixture of oxygen and nitrogen (12.7 mm I.D.), an intermediate annular bronze

porous plug used for supplying the fuel (30 mm I.D.), and an outer bronze porous plug (75 mm I.D.)

for a nitrogen stream that was used as a shield to prevent the formation of secondary flames with the

room air. The burner assembly was mounted on a lifting platform for accurate movement in the vertical

direction to adjust the sampling location. Liquid fuel (n-heptane) was vaporized and mixed with argon

at 423 K using a W-102A Bronkhorst vapor delivery system. The mixture was transferred to the burner

through heated tubes maintained at 473 K. To prevent fuel condensation inside the burner, the gaseous

mixture of oxygen and nitrogen, and shielding nitrogen were heated to 423 K using a coil heater. The

fuel (n-heptane) and carrier gas (Ar) flow rates set by Bronkhorst digital flow controllers were 70 g/h

(±0.02%) and 0.31 L/min (±0.2%), respectively, at 273.15 K. The flow rates of oxygen, nitrogen and

shielding nitrogen were 0.52, 0.6 and 55 L/min at 293.15 K, respectively, which were set by digital

mass flow controllers with accuracy of ±0.2%. Under these operating conditions, the visible flame

height was 60 mm as shown in Fig. S2 of Supplemental material.
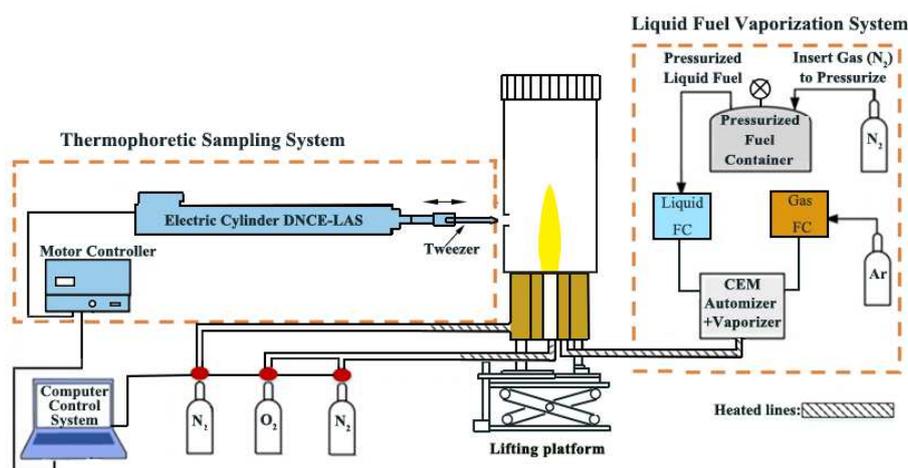
Fig. S1. Schematic diagram of the experimental system.
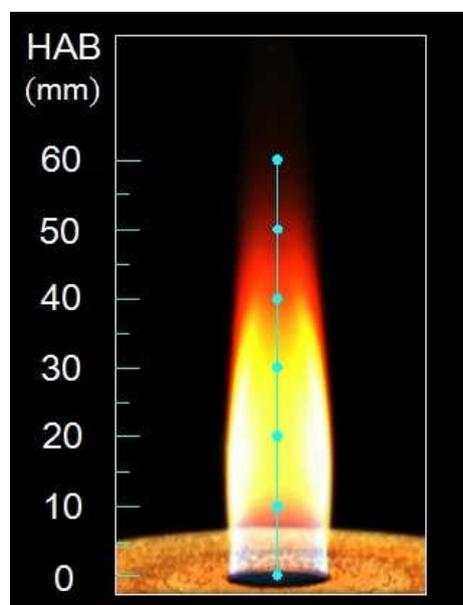
Fig. S2. Flame photo and measuring positions.

A thermophoretic sampling technique was used to extract soot samples for subsequent PF-TUNA

and KPFM analyses. The residence time for the thermophoretic sampling was 30 ms. The instrument

incorporated an advanced linear electrical cylinder (FESTO, Germany) that allowed for a precise and

rapid reciprocating motion. The piston rod was attached to self-closing tweezers (N5, Switzerland) to

conveniently fix and detach the substrate. The thermophoretic sampling technique has been described

previously in detail [13]. Gold substrates were prepared by evaporating 500-nm-thick Au onto heated

mica in a 10^{-5}-Torr vacuum. A gold substrate and a highly oriented pyrolytic graphite (HOPG, ZYH

grade, SUA) substrate were used to obtain soot particles at different heights above the burner (HAB).

The sampling conditions in the present experiments are summarized in Table 1. Sampling process was

repeated five times at each HAB to obtain the measurement uncertainty. In addition, a Teflon filter was

used to collect soot samples for subsequent XPS and XRD analyses using the probe sampling

technique. A detailed description of the probe sampling technique has been reported previously [14].

To evaluate the impact of the sampling methods on soot sample structure, a quartz plate was used on

thermophoreric sampling system, and was subject to insertion in the flame many times to obtain an

amount of soot for the XRD analysis. It was found that the XRD patterns of soot obtained with the

thermophoretic sampling technique were quite similar to those with the probe sampling technique,

demonstrating that the soot sampling methods have little impact on soot structure. The temperature

along the centerline direction of the flame was measured by a fast insertion procedure using an R-type

thermocouple (Pt/Pt−13% Rh) with a 30-µm wire and a bead diameter of approximately 150 µm. The

temperature values thus obtained were corrected for radiative heat loss [15], and the uncertainty in the

flame temperature measurements was determined to be no greater than ±50 K.

Table 1

Experimental sampling conditions

Sampling positions (mm)	Flame temperature of sampling position (K)
HAB = 10	1386 ± 50
HAB = 20	1546 ± 50

HAB = 30	1375 ± 50
HAB = 40	1161 ± 50

1 *2.2. PF-TUNA*

2 The quantitative conductive property of an isolated soot particle was measured using a Dimension

3 Icon AFM (Bruker, USA) with a Nanoscope V controller and PF-TUNA module under ambient

4 conditions. The PF-TUNA probes had Ti/Pt-coated tips with spring constant 2 N/m and resonance

5 frequency 70 kHz (OSCM-PT-R3, Bruker). Conductive silver paint (G3790, Agar Scientific) was used

6 to attach the base of the HOPG substrate to a steel disc and to make an electrical contact between this

7 disc and the soot samples, which enabled a bias to be applied between the grounded sample and the

8 AFM tip. The HOPG was selected as a substrate owing to its high conductivity nature, which had a

9 negligible impact on the current–voltage (I–V) curve measurements of the soot samples [16,17]. For

10 I–V curve measurements, first, a topographical image of the soot particles on the HOPG substrate was

11 acquired over an area of 1 μm × 1 μm to locate isolated soot particles. Then, I–V curve measurements

12 were performed using the point and shoot feature at the selected particles and repeated at least three

13 times for each selected particle under the same conditions. Isolated soot particles with circular bottoms

14 were used for the I–V curve measurements to avoid interference from other soot particles. For each

15 sample, more than 150 isolated soot particles were selected to obtain statistically significant results.

16 *2.3. KPFM*

17 KPFM measurements were carried out using a Dimension Icon AFM equipped with a Nanoscope

18 V controller. The tips used were commercial cobalt-chromium-coated Si cantilevers with spring

19 constant 2.8 N/m. All KPFM measurements were carried out at room temperature inside a glovebox

20 with relative humidity less than 4% to eliminate the possible effects of a water film on the sample

surface. To obtain the KPFM images, each scan consisted of two passes. The first pass was a tapping

mode AFM scan with no external voltage applied. Next, the tip was lifted up to 100 nm above the

sample and scanned at a constant height during the second pass, while a variable DC or AC voltage

was applied to the tip. The surface potential ($\Delta\Phi_{\text{tip-sample}}$) of the soot particle sample, that is, $\Delta\Phi_{\text{tip-sample}}$

$= \Phi_{\text{tip}} - \Phi_{\text{sample}}$, was the average from the KPFM image [3]. Then, the work function of the sample was

then given by $\Phi_{\text{sample}} = \Phi_{\text{tip}} - \Delta\Phi_{\text{(tip-HOPG)}}$. The results of the work function from three different sections

of each soot sample were averaged to ensure reproducibility.

2.4. XRD, XPS and HRTEM

The crystallite parameters of the soot particles were determined using a Rigaku D/MAC/max

2500v/pc powder XRD with Cu Kα radiation (40 kV, 200 mA, λ = 1.5406 Å). The scan range of 5°–

110° was used with scan step size of 0.02° and scan speed of 10 s/step. XPS spectra were recorded on

a PerkinElmer PHI-1600 ESCA spectrometer using a Mg Kα X-ray source. The binding energies were

calibrated using the C 1-s peak of contaminant carbon (BE = 284.6 eV) as an internal standard. An

HRTEM (Philips Tecnai F20) with a point resolution of 0.248 nm operating at 200 kV was used to

obtain HRTEM and TEM images.

3. Results and discussion

3.1. Electrical conductivity

Measurements of the *I–V* curves were performed on the selected isolated particles, and the applied

bias voltage ranging from −0.4 to +0.4 V. Figure 1 shows a representative *I–V* curve for an isolated

particle labeled in the topographical image. The *I–V* curve exhibits a non-ohmic electrical behavior.

Based on the *I–V* curves, the electrical conductivity (σ′) was calculated using Eq. (1) [9]:

$$\sigma' = G\frac{4H}{\pi D^2} \tag{1}$$

where G is the electrical conductance, calculated from the slope of the I–V curves in the interval

between 0.2 and 0.4 V [9]. H is the selected particle height and D is the bottom diameter of the selected

particle. The values of H and D were obtained from the topographical images using scanning probe

image processor software according to the procedure proposed by Barone et al. [18]. For each sample,

more than 150 isolated soot particles were measured to obtain statistical significance. The mean values

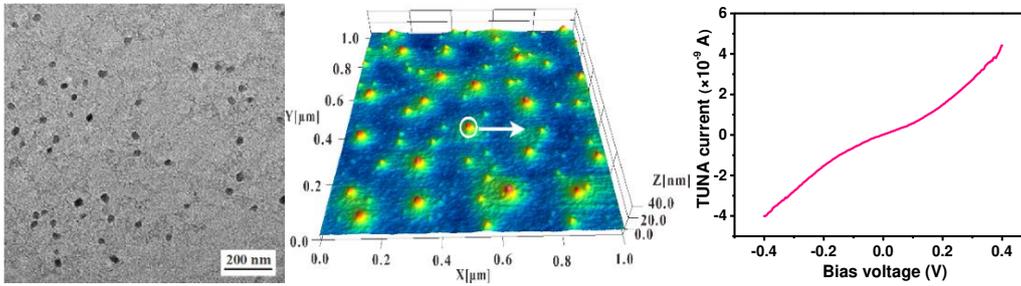of H and D are shown in Fig. S3 of Supplemental material.

Fig. 1. Representative TEM and AFM images and I−V curve recorded from point labeled in the
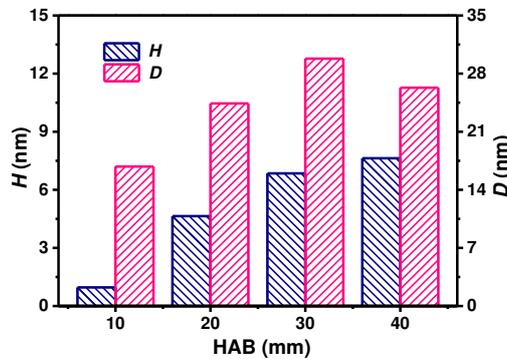
AFM image (HAB=20 mm).

Fig. S3. Mean values of the soot particle height (H) and bottom diameter (D) at various HAB values.

Figure S4 of Supplemental material shows the σ′ distributions for the soot particle samples. The

range values of the σ′ distribution widened as the HAB increased from 10 to 40 mm. For example, at

the low HAB value of 10 mm, the σ′ values were distributed in the range of 0.03–0.37 S/cm, whereas

the σ′ values at the high HAB value of 40 mm were in the range of 2.48–453.28 S/cm. Correspondingly,

the mean electrical conductivity ($\overline{\sigma'}$) shown in Fig. 2 increased from 0.11 to 205.01 S/cm, which was

an increase of three orders of magnitude. These results demonstrate that the electrical conductivity of

soot particles increases significantly as they matured. De Falco et al. [9] studied the electrical

conductivity of bulk soot particles formed in an ethylene premixed flame. They found that the electrical

conductivity was in the range of 0.004–115 S/cm, which was lower than our results. This difference is

likely due to two factors. First, for the bulk soot particles, the electrical conductivity was affected not

only by intra-soot particle conduction, but also by inter-soot particle conduction [19]. Second, the

different parent fuel and synthesis conditions led to the differences in the soot physiochemical

properties, and thus the soot particles exhibit different electrical conductivity. To estimate the impact

of soot particle size on the electrical conductivity, more than 150 individual soot particles at HAB =

40 mm were measured in terms of size and electrical conductivity. The average values of electrical

conductivity for the soot particles in the sizes of 14-16, 17-19, 20-22 nm are 177.63, 253.18, and

208.65 S/cm, respectively. These results suggest that there is not a definite correlation between the

electrical conductivity and size.
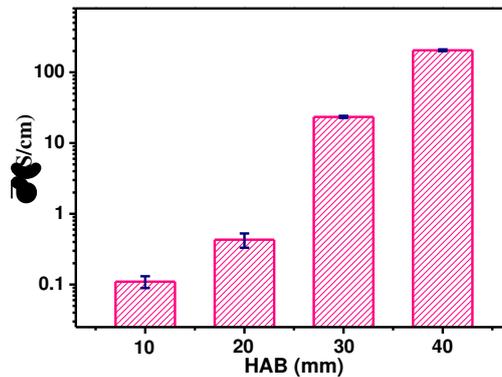
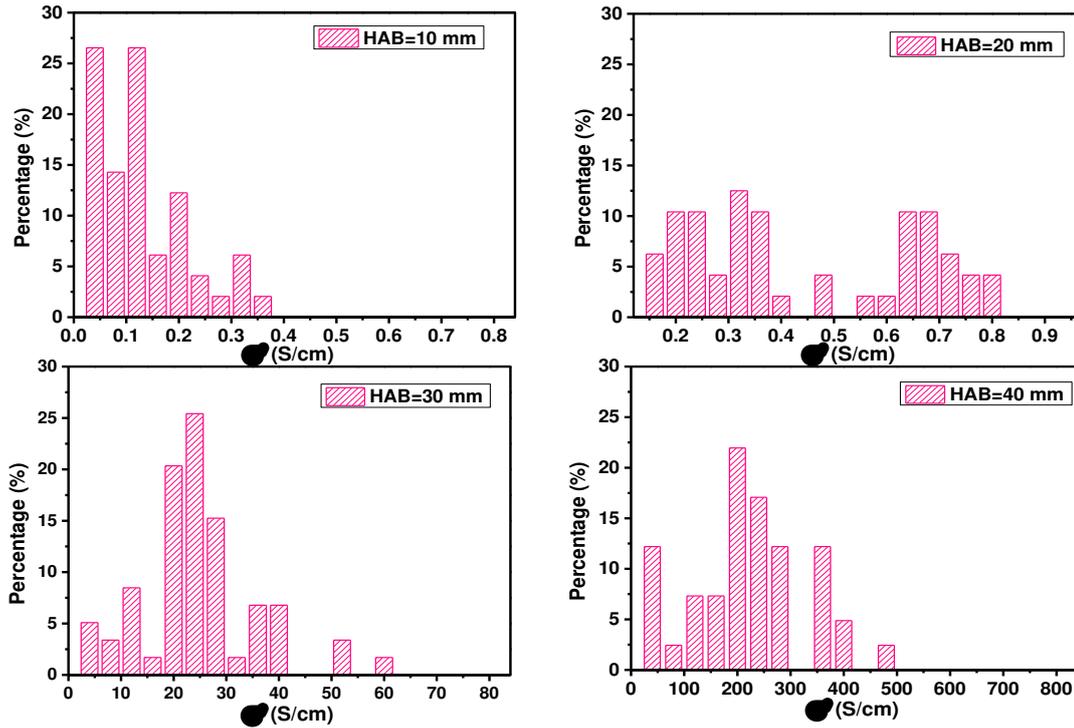Fig. 2. Mean electrical conductivity ($\overline{\sigma'}$) for the soot particles at various HAB values.

Fig. S4. Distributions of the electrical conductivity (σ′) for soot particles at various HAB values.

It is interesting to note in Fig. 2 that when HAB increased from HAB = 20 mm to HAB = 30 mm, the $\overline{\sigma'}$ increased by approximately two orders of magnitude. In contrast, either from HAB = 10 mm to HAB = 20 mm or from HAB = 30 mm to HAB = 40 mm, the $\overline{\sigma'}$ increased only by less than one order of magnitude. Such a behavior is likely to have arisen from reaching the percolation threshold of the percolation theory for soot particles [2,20]. It is believed that when the volume fraction of conductive crystallites in a carbon material reaches a critical volume fraction, that is, the percolation threshold, the conductive crystallites will assist in electron hopping and tunneling, which results in a sharp increase in the $\overline{\sigma'}$ [21-23]. Rhim et al. [2] reported that reaching the percolation threshold contributes to the greatest increase, by two orders of magnitude, in the electrical conductivity for microcrystalline cellulose. In studies of graphite flakes by Celzard et al. [24] and of carbon black by McLachlan et al. [25], such a conductivity behavior was found to be increased by three to four orders of magnitude when reaching the percolation threshold. In addition, the soot particle samples were

12

extracted with dichloromethane in Soxhlet apparatus for 24 h to remove off the soluble organic fraction on soot surface. The *I–V* curves for the samples after extraction were measured. A slight difference within experimental error was found in electrical conductivity between the soot particles before and after Soxhlet extraction, indicating that the effect of the soluble organic fraction on the electrical conductivity can be ignored.
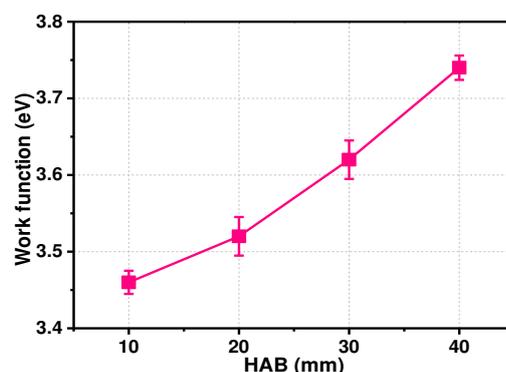
3.2. Work function

The KPFM technique was employed to investigate the work function of the soot samples. Prior to measurement, a Co/Cr-coated tip and a freshly cleaved HOPG reference sample were used for calibration. The work function (Φ_{HOPG}) of the HOPG in air is 4.65 eV [26]. The surface potential ($\Delta\Phi_{tip\text{-}HOPG}$) of a freshly cleaved HOPG was measured to be 0.11 ± 0.01 eV. From this value, the work function of a Co/Cr coating tip was determined to be $\Phi_{tip} = \Delta\Phi_{tip\text{-}HOPG} + \Phi_{HOPG} = 4.76 \pm 0.01$ eV, which matched well with a previously reported result of 4.75 ± 0.03 eV [27]. After calibration, the work function of the gold substrate was measured to confirm the reliability of this measurement methodology. The Φ_{gold} value obtained was 4.93 ± 0.02 eV, which was in good agreement with the values in the range of 4.8–5.2 eV reported previously [3,28]. Therefore, KPFM analysis can be used to accurately measure the work function of soot particles.

During sampling, the gold substrate on the thermophoretic sampling was subject to insertion in the flame many times so that the gold substrate was completely covered by soot samples to rule out any effect that the gold substrate might have on measurements. Figure 3 displays typical KPFM image for soot particles deposited on a gold substrate. The work function was obtained from the surface potential, while the surface potential could be reflected by the brightness on the KPFM image. Owing to the coexistence of young and mature soot particles in the sample, the distributions of the brightness

13

were not uniform in Fig. 3. Therefore, the mean values were used to characterize the work function of soot particles. The mean values of work function for the soot samples are shown in Fig. 4. The work function shows a gradual increase from 3.46 to 3.74 eV in response to the HAB increasing from 10 to 40 mm, which suggests that it became difficult for electrons to escape from the soot samples as the soot particles gradually aged. Similar to the $\overline{\sigma'}$, there was a slight difference within the range of experimental error in the work function between the soot particles before and after Soxhlet extraction. This indicates that the effect of the soluble organic fraction on the work function can be ignored.
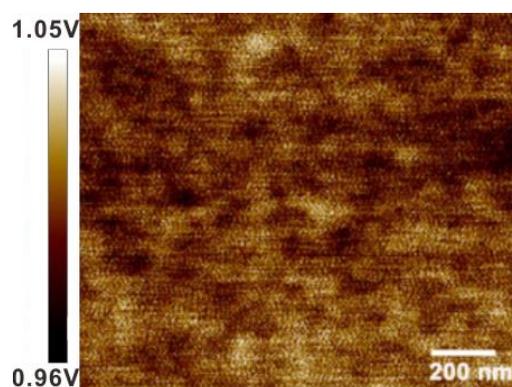
Fig. 3. Typical KPFM image for soot particles deposited on a gold substrate (HAB = 40 mm).

Fig. 4. Work function as a function of HAB. The error bars indicate the standard error.

3.3. Soot nanostructure

XRD analyses were performed to obtain quantitative information about the crystalline structure of the soot samples. Figure 5 shows the XRD patterns of the soot particle samples. The XRD patterns were fitted by Gaussian function to obtain the full width at half maximum (FWHM) and the angles of

1   (100) and (002) peaks. The interlayer spacing (d_{002}), the crystallite height (L_c), and the crystallite width

2   (L_a), were calculated from the XRD pattern using a previously reported method [29-31]. To estimate

3   the fringe number within the primary soot particle, more than 100 primary soot particles were

4   randomly selected from the HRTEM images at each HAB, and the fringe number was obtained using

5   the lattice fringe analysis [32].
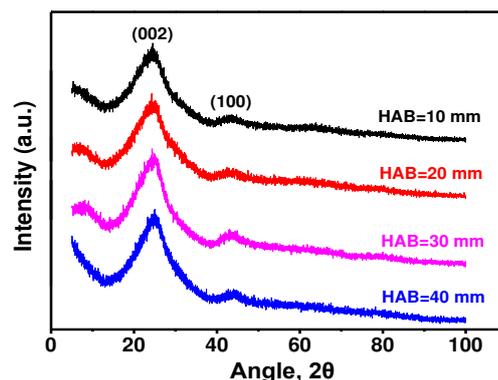
6
7   Fig. 5. X-ray diffraction (XRD) pattern of the soot particles at various HAB values.

8   Table 2 provides the values of the structural parameters. Both the L_a and L_c increase with

9   increasing HAB values, while the d_{002} and the fringe number decrease. These results demonstrate the

10   soot evolution towards better graphitic organization. In addition to the quantification of the structure

11   parameters in terms of d_{002}, L_a, L_c, and fringe number using XRD and HRTEM analyses, XPS was

12   employed to supplement the structure information and validate the XRD results. Figure 6 shows a

13   typical high-resolution scan of the C 1-s peaks. The C 1-s region was deconvoluted to five peaks

14   according to the method reported in the literatures [33,34]. The π–π stack at 290.5 eV corresponds to

15   the ordered graphene layers. The sp^2 hybridized carbon at 284.5 eV was attributed to graphitic carbon

16   within the basal plane, and is representative of π bonding in soot, while the sp^3 hybridized carbon at

17   285.3 eV is a class of defects that can disrupt the sp^2 hybridized network, and is representative of σ

18   bonding in soot [30,33]. Therefore, a large sp^2/sp^3 ratio indicates a high quantity of aromatic

19   hydrocarbons (π bonding) and a low amount of cyclic or acyclic aliphatics (σ bonding) in the soot

15

particles [29]. As expected, the sp^2/sp^3 ratio for the soot particles shows an increasing trend with an

increase in the HAB values. At the same time, the content of the π–π stack increased from 4.88% to

9.86% (see Table 2). These XPS results indicate an increase in the graphitic character of the soot

particle samples, in line with the preceding XRD data.

Table 2

Structural parameter obtained from XRD, HRTEM and XPS analyses.

| HAB (mm)	d_{002} (Å)	L_c (Å)	L_a (Å)	fringe number	sp^2/sp^3 ratio	π–π (%)
10	3.679±0.005	10.33±0.06	22.50±0.67	1383±45	1.58±0.05	4.88±0.18
20	3.667±0.005	10.57±0.05	24.72±0.57	1123±58	1.69±0.04	6.28±0.24
30	3.639±0.004	10.70±0.06	27.57±0.61	911±50	2.01±0.05	7.85±0.21
40	3.617±0.004	10.87±0.07	29.07±0.76	731±51	2.11±0.06	9.86±0.25
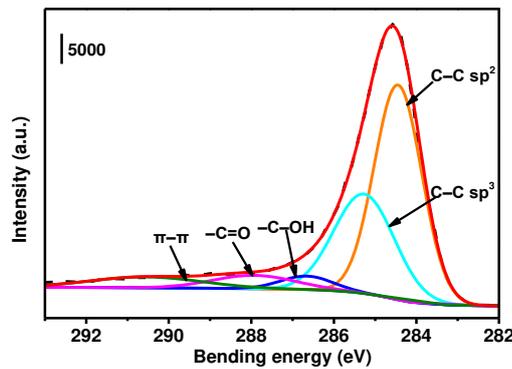
Fig. 6. Typical XPS C 1-s narrow spectra (HAB=20 mm).

3.4. Correlations between the electrical properties and soot nanostructure

3.4.1. Electrical conductivity and nanostructure

To establish a possible correlation, the obtained values of L_a and d_{002} as functions of the logarithm

(base 10) of electrical conductivity ($\log \overline{\sigma'}$) are plotted in Fig. 7 for the soot samples. It is obvious that

there is a positive correlation between the L_a and $\log \overline{\sigma'}$ and a negative correlation between the d_{002} and

$\log \overline{\sigma'}$. That is, the values of $\log \overline{\sigma'}$ increase with increasing L_a or with decreasing d_{002}. The linear

correlation coefficients R^2, calculated by simple linear regression, are 0.96 for L_a versus $\log \overline{\sigma'}$, and

0.98 for d_{002} versus $\log \overline{\sigma'}$. It is believed that the electrical conductivity of the carbonaceous materials

1   is governed by the size of the conductive carbon clusters. The conductive carbon clusters here refers

2   to the graphene layers (fringes), which are often defined in terms of L_a and d_{002} [2,21,35]. A decrease

3   in d_{002} means a shrinkage of the carbon monolithic structure, thereby reducing the distance between

4   the conductive carbon clusters, which facilitates electrons hopping from one carbon cluster to

5   neighboring clusters. In addition, the increase in L_a suggests an increase in the content of π–π stacks,

6   and thus more delocalized π electron systems form, which will give rise to an increase in the number

7   of π electrons [36]. As a consequence, the electrical conductivity for soot particles increases sharply

8   [2,36].
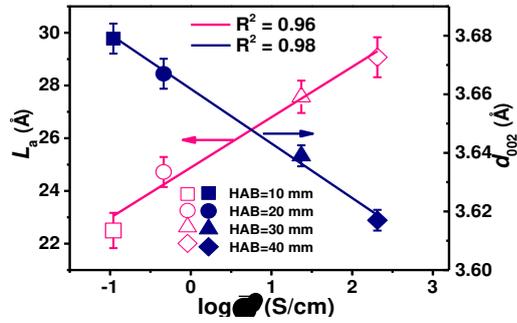
10   Fig. 7. Crystallite width (L_a) and interlayer spacing (d_{002}) as functions of the logarithm (base 10)

11   of electrical conductivity. The error bars indicate the standard error.

12   The increase in electrical conductivity by the growth and interconnectivity of the carbon clusters

13   can be described by percolation theory [2,21]. The percolation model used was as follows [37]:

14
$$I = C\left(\frac{A-BV}{\exp\{(A-BV)/T\}-1} - \frac{A+BV}{\exp\{(A+BV)/T\}-1}\right) \qquad (2)$$

15   where A is associated with an activation energy (E_a) of the charge transfer process, $A = E_a/k$, where k

16   is the Boltzmann constant. B is a constant dependent on the temperature and the material, and C is the

17   exponential dependence on the distance between carbon clusters [21].

18   Equation (2) at 298 K was used to fit the experimental I–V curves using Matlab software. All the

19   model I–V curves show a good fit with the experimental I–V curves. The representative experimental

1 and model I–V curves for an isolated soot particle are shown in Fig. S5 of Supplemental material. The

2 values of A, B and C were obtained by fitting the experimental data with the non-linear fitting method,

3 and average data of A and C are listed in Table 3. The E_a values, evaluated by $E_a = A \times k$, are also listed

4 in the Table 3. As HAB increases from 10 to 40 mm, a nearly exponential increase in the mean of the

5 C values indicates a decreased distance between carbon clusters, which agrees with the preceding XRD

6 results. Moreover, the decrease in E_a values, when increasing HAB from 10 to 40 mm, indicates that

7 the charge moved easily inside soot, which is reflected in the increase in electrical conductivity.
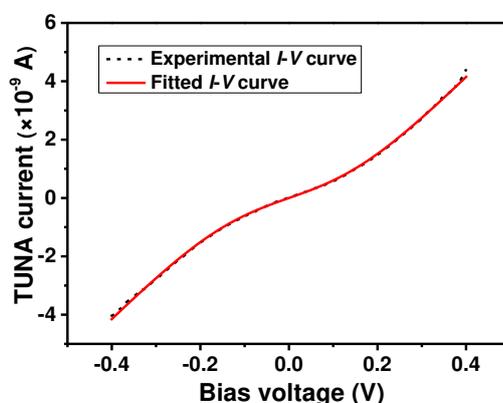
9 Fig. S5. Representative experimental and fitted I–V curves
10 for an isolated soot particle (HAB=20 mm).

11 **Table 3**

12 Average A and C, and E_a obtained from the fitted I-V curves
13 for the soot particles at various HAB values.

HAB (mm)	A (K)	C (A/K)	E_a (meV)
10	717.9±26.3	$(2.0\pm0.2)\times10^{-12}$	61.9±2.2
20	652.5±20.8	$(2.7\pm0.2)\times10^{-12}$	56.3±1.8
30	541.3±18.7	$(8.5\pm0.3)\times10^{-10}$	46.7±1.6
40	486.3±24.4	$(1.4\pm0.1)\times10^{-8}$	41.9±2.1

15 *3.4.2. Work function and nanostructure*

16   The values of L_a and d_{002} against the work function are plotted in Fig. 8. There is an evident

17 positive correlation between L_a and work function, whereas there is a negative correlation between

18 d_{002} and work function. The R^2 values are 0.92 for L_a versus work function, and 0.99 for d_{002} versus

1   work function. Theoretically, the increase in L_a and the decrease in d_{002} correspond to increased π

2   bonding and decreased σ bonding in soot, which consequently reduced the number of defect sites

3   where localized electrons formed [38]. On the other hand, an increase in L_a and a decrease in d_{002}

4   suggest an increase in the content of the π–π stack [30,31]. The increase in the content of the π–π stack

5   improves the formation of delocalized π electron systems, and thereby increasing the number of

6   delocalized electrons [7]. The increased content of the π–π stack also leads to a substantial

7   intermolecular π–π overlap of the electronic wavefunctions, which in turn contributes to an increase

8   in the depth of the attractive potential inside the soot [39]. These two factors strengthen electron

9   binding in soot, increasing the work function for the soot particles [40]. This assertion is supported by

10 a comparison between the HOPG and soot particles. As compared with soot particles, the HOPG

11 possesses a larger π–π overlap of the electronic wavefunctions and more delocalized electrons in the

12 graphite crystal. Correspondingly, the HOPG exhibits a higher work function (4.65 eV) [26]. Palermo

13 et al. [3] studied the work function of the layer and network architectures of nanographene, and they

14 found that the layer architecture with more delocalized electrons along the π–π stacks exhibited a

15 higher work function.
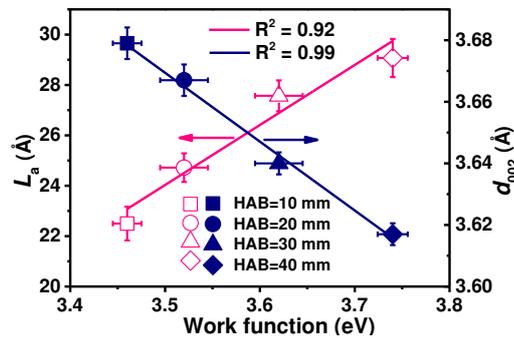
17 Fig. 8. Crystallite width (L_a) and interlayer spacing (d_{002}) as functions of the work function.

18 The error bars indicate the standard error.

19 **4. Conclusions**

The electrical properties of soot particles and the relationship between these electrical properties and the nanostructure of the soot particles were studied using an n-heptane inverse diffusion flame. The electrical conductivity exhibits different distributions as the soot particles mature. Correspondingly, the mean electrical conductivity increases by three orders of magnitude. The electrical conductivity of soot particles shows a steep increase when the percolation threshold is reached, which follows percolation theory. The work function of soot particles increases during the maturation process, implying that it becomes more difficult for electrons to escape from the soot samples. The crystallite width has a positive correlation with the logarithm of the electrical conductivity and work function for the soot particles, whereas the interlayer spacing has a negative correlation with the logarithm of electrical conductivity and work function. These results suggest that the electrical conductivity and work function can serve as indicators of ordering degree of soot particles. Furthermore, the dependence of electrical properties on the nanostructure demonstrates the potential of better controlled flame conditions for producing tailored soot particles for a variety of applications.

Acknowledgments

References

[1] M.E. Spahr, D. Goers, A. Leone, S. Stallone, E. Grivei, J. Power Sources 196 (7) (2011) 3404-3413.

[2] Y.R. Rhim, D. Zhang, D.H. Fairbrother, K.A. Wepasnick, K.J. Livi, R.J. Bodnar, D.C. Nagle, Carbon 48 (4) (2010) 1012-1024.

[3] V. Palermo, M. Palma, Z. Tomovic, M.D. Watson, R. Friedlein, K. Mullen, P. Samori, ChemPhysChem 6 (11) (2005) 2371-2375.

[4] Z. Yao, H.W.C. Postma, L. Balents, C. Dekker, Nature 402 (6759) (1999) 273-276.

[5] Y.S. Kim, S.C. Ha, Y. Yang, Y.J. Kim, S.M. Cho, H. Yang, Y.T. Kim, Sens. Actuators B 108 (1-2) (2005) 285-291.

[6] C.A. Frysz, X. Shui, D.D.L. Chung, J. Power Sources 58 (1) (1996) 41-54.

[7] V. Palermo, M. Palma, P. Samorì, Adv. Mater. 18 (2) (2006) 145-164.

[8] T.W. Odom, J.L. Huang, P. Kim, C.M. Lieber. Atomic structure and electronic properties of single-walled carbon nanotubes. Nature 391 (6662) (1998) 62-64.

[9] G. De Falco, M. Commodo, C. Bonavolontà, G.P. Pepe, P. Minutolo, A. D'Anna, Combust. Flame 161 (12) (2014) 3201-3210.

[10] B. Grob, J. Schmid, N.P. Ivleva, R. Niessner, Anal. Chem. 84 (8) (2012) 3586-3592.

[11] L.G. Blevins, R.A. Fletcher, B.A. Benner, E.B. Steel, G.W. Mulholland, Proc. Combust. Inst. 29 (2) (2002) 2325-2333.

[12] A. Santamaria, N. Yang, E. Eddings, F. Mondragon, Combust. Flame 157 (1) (2010) 33-42.

[13] Y. Liu, C. Song, G. Lv, N. Chen, H. Zhou, X. Jing, Appl. Surf. Sci. 433 (2018) 450-457.

[14] Y. Liu, C. Song, G. Lv, X. Wang, N. Li, Energy Fuels 31 (6) (2017) 6413-6421.

[15] C.S. McEnally, Ü. Ö. Köylü, L.D. Pfefferle, D.E. Rosner, Combust. Flame 109 (4) (1997) 701-720.

[16] G.W. Zajac, J.M. Gallas, A.E. Alvarado-Swaisgood, J. Vac. Sci. Technol. B 12 (3) (1994) 1512-1516.

[17] W. Rivera, , J.M. Perez, R.S. Ruoff, D.C. Lorents, R. Malhotra, S. Lim, R.F. Pinizzotto, J. Vac. Sci. Technol. B 13 (2) (1995) 327-330.

[18] A.C. Barone, A. D'Alessio, A. D'Anna, Combust. Flame 132 (1) (2003) 181-187.

[19] J. Sánchez-González, A. Macías-García, M.F. Alexandre-Franco, V. Gómez-Serrano, Carbon 43(4) (2005) 741-747.

[20] S. Barrau, P. Demont, A. Peigney, C. Laurent, C. Lacabanne, Macromolecules 36 (14) (2003) 5187-5194.

[21] A.K. Kercher, D.C. Nagle, Carbon 42 (1) (2004) 219-221.

[22] C. Godet, Diamond Relat. Mater. 12 (2) (2003) 159-165.

[23] S. Hussain, I. Barbariol, S. Roitti, O. Sbaizero, J. Eur. Ceram. Soc. 23 (2) (2003) 315-321.

[24] A. Celzard, E. McRae, C. Deleuze, M. Dufort, G. Furdin, J.F. Marêché, Phys. Rev. B 53 (10) (1996) 6209-6214.

[25] D.S. McLachlan, M.B. Heaney, Phys. Rev. B 60 (18) (1999) 12746-12751.

[26] C. Sommerhalter, T.W. Matthes, T. Glatzel, A. Jäger-Waldau, M.C. Lux-Steiner, Appl. Phys. Lett. 75 (2) (1999) 286-288.

[27] Jiang, T.D. Krauss, L.E. Brus, J. Phys. Chem. B 104 (50) (2000) 11936-11941.

[28] H.O. Jacobs, A. Stemmer, Surf. Interface Anal. 27 (1999) 361-367.

[29] G.D.J. Guerrero Peña, A. Raj, S. Stephen, T. Anjana, Y.A.S. Hammid, J.L. Brito, A.A. Shoaibi, Combust. Flame 178 (2017) 286-296.

[30] G.D.J. Guerrero Peña, M.M. Alrefaai, S.Y. Yang, A. Raj, J.L. Brito, S. Stephen, T. Anjana, V. Pillai, A. Al Shoaibi, S.H. Chung, Combust. Flame 172 (2016) 1-12.

[31] B. Gogoi, A. Raj, M.M. Alrefaai, S. Stephen, T. Anjana, V. Pillai, S. Bojanampati, Fuel 159 (2015) 766-775.

[32] Z. Li, C. Song, J. Song, G. Lv, S. Dong, Z. Zhao. Combust. Flame 158(8) (2011) 1624-1630.

[33] C.K. Gaddam, R.L. Vander Wal, Combust. Flame 160 (11) (2013) 2517-2528.

[34] M. Pumera, H. Iwai, J. Phys. Chem. C 113 (11) (2009) 4401-4405.

[35] Y.R. Rhim, D. Zhang, M. Rooney, D.C. Nagle, D.H. Fairbrother, C. Herman, D.G. Drewry, Carbon 48 (1) (2010) 31-40.

[36] Z.R. Yue, W. Jiang, L. Wang, S.D. Gardner, C.U. Pittman, Carbon 37 (11) (1999) 1785-1796.

[37] P. Bruschi, A. Nannini, Thin Solid Films 201 (1) (1991)29-38.

[38] P. Stallinga, Adv. Mater. 23 (30) (2011) 3356-3362.

[39] R. Friedlein, X. Crispin, C.D. Simpson, M.D. Watson, F. Jäckel, W. Osikowicz, S. Marciniak, M.P. de Jong, P. Samorí, S.K.M. Jönsson, M. Fahlman, K. Müllen, J.P. Rabe, W.R. Salaneck, Phys. Rev. B 68 (19) (2003) 195414

[40] M. Prutton, Introduction to Surface Physics, Oxford University Press, Oxford, 1994, p. 139.

Figure captions

Fig. 1. Representative TEM and AFM images and $I−V$ curve recorded from point labeled in the AFM image (HAB=20 mm).

Fig. 2. Mean electrical conductivity ($\bar{\sigma'}$) for the soot particles at various HAB values.

Fig. 3. Typical KPFM image for soot particles deposited on a gold substrate (HAB = 40 mm).

Fig. 4. Work function as a function of HAB. The error bars indicate the standard error.

Fig. 5. X-ray diffraction (XRD) pattern of the soot particles at various HAB values.

Fig. 6. Typical XPS C 1-s narrow spectra (HAB=20 mm).

Fig. 7. Crystallite width (L_a) and interlayer spacing (d_{002}) as functions of the logarithm (base 10) of electrical conductivity. The error bars indicate the standard error.

Fig. 8. Crystallite width (L_a) and interlayer spacing (d_{002}) as functions of the work function. The error bars indicate the standard error.

1 **Supplementary materials**

2 Fig. S1. Schematic diagram of the experimental system.

3 Fig. S2. Flame photo and measuring positions.

4 Fig. S3. Mean values of the soot particle height (*H*) and bottom diameter (*D*) at various HAB values.

5 Fig. S4. Distributions of the electrical conductivity for soot particles at various HAB values.

6 Fig. S5. Representative experimental and fitted *I–V* curves for an isolated soot particle (HAB=20 mm).